

Journal of
**Micro/Nanolithography,
MEMS, and MOEMS**

Nanolithography.SPIEDigitalLibrary.org

**Optical microlithography on oblique
and multiplane surfaces using
diffractive phase masks**

Peng Wang
Rajesh Menon

Optical microlithography on oblique and multiplane surfaces using diffractive phase masks

Peng Wang and Rajesh Menon*

University of Utah, Department of Electrical and Computer Engineering, Salt Lake City, Utah 84112, United States

Abstract. Micropatterning on oblique and multiplane surfaces remains a challenge in microelectronics, microelectromechanics, and photonics industries. We describe the use of numerically optimized diffractive phase masks to project microscale patterns onto photoresist-coated oblique and multiplane surfaces. Intriguingly, we were able to pattern a surface at 90 deg to the phase mask, which suggests the potential of our technique to pattern onto surfaces of extreme curvature. Further studies show that mask fabrication error of below 40-nm suffices to conserve pattern fidelity. A resolution of 3 μm and a depth-of-focus of 55 μm are essentially dictated by the design parameters, the mask generation tool, and the exposure system. The presented method can be readily extended for simple and inexpensive three-dimensional micropatterning. © The Authors. Published by SPIE under a Creative Commons Attribution 3.0 Unported License. Distribution or reproduction of this work in whole or in part requires full attribution of the original publication, including its DOI. [DOI: [10.1117/1.JMM.14.2.023507](https://doi.org/10.1117/1.JMM.14.2.023507)]

Keywords: microlithography; optical lithography; diffractive optics; mask; optimization.

Paper 15003 received Jan. 20, 2015; accepted for publication Apr. 29, 2015; published online May 22, 2015.

1 Introduction

Microstructures on oblique and nonplanar surfaces enable unique functionalities in photonics,^{1,2} electronics,³ and microelectromechanics,^{4,5} and provide a broad array of interesting applications in high-gain antennas,⁶ radio-frequency identification devices,⁷ metamaterials,⁸ and transformation optics.⁹ For instance, combining diffractive microstructures atop a curved refractive surface can minimize aberrations in lenses, in a more compact way compared to the conventional methods by adaptive optics.¹⁰ In addition, micropatterning on the sidewalls of implantable neural probes could potentially lead to an effective approach of recording three-dimensional (3-D) neural signals.^{11,12} Meanwhile, shape modification in the vertical direction of microfluidic channels and 3-D integration may significantly enhance their performances.^{5,13}

Optical projection lithography (OPL) on planar silicon substrates is the workhorse of the semiconductor industry due to its high throughput, resolution, and accuracy.¹⁴ In OPL, a photomask pattern is imaged with demagnification onto a planar photoresist layer that coats the silicon substrate. In general, it is difficult to utilize OPL to pattern nonplanar or oblique surfaces due to the limitations of the imaging optics. These limitations can be avoided by lens-less lithography that utilizes computer-generated holograms (CGHs) to directly project patterns onto the photoresist surface.¹⁵ Thus far, these approaches only project the pattern onto a single plane surface. In this paper, we extend this technique by designing diffractive optics that can manipulate the intensity of light in 3-D space, and thereby allow for patterning onto nonplanar and oblique surfaces. An alternative approach for lithography on nonplanar and oblique surfaces is to utilize a flexible template that contains a master pattern and apply this template conformally over the substrate. The pattern may be transferred via an imprint process^{16–18} or simply by exposure

to ultra-violet (UV) light through the template.¹⁹ These approaches require contact with the substrate surface, which increases the potential for damage, increases defects, and reduces yield. Furthermore, these approaches perform well only for surfaces of small curvature since conformal contact is necessary. In contrast, our approach can be applied to surfaces of extreme curvature as illustrated by patterning of a substrate that is placed orthogonal to the diffractive mask.

2 Lithography Principle

Our approach is schematically explained in Fig. 1. A spatially collimated, temporally coherent uniform UV beam illuminates the mask [see Fig. 1(a)]. The sample to be exposed is placed at a specified distance behind the mask, where the light intensity distribution in three dimensions is controlled. The mask is designed using an enhanced direct-binary-search algorithm,^{20–26} where the optimization objective is to maximize intensity within prescribed patterns in multiple planes or within a 3-D volume. This numerical technique was successfully implemented in designing various diffractive-optical elements.^{27,28} In addition, the intensity uniformity within the target image has to be taken into account. Note that in optical lithography, the (positive-tone) photoresist serves as a nonlinear recording medium, where regions receiving energy higher than a threshold are selectively dissolved away in a developer. Hence, the mask only needs to ensure that the desired regions receive energy (which corresponds to light intensity multiplied by the exposure time) above a certain threshold (defined by the sensitivity of the photoresist at the exposure wavelength). The resulting mask comprised an array of discrete pixels, either in one dimension (along the X direction) or two dimensions (on the XY plane), where each pixel in the array applies a phase shift to the incident light. This resembles a traditional CGH, which is usually used to generate complex beams or images.²⁹ The phase shift of each pixel is controlled during optimization. The array of optimal phase shifts is implemented as an array of pixels with varying

*Address all correspondence to: Rajesh Menon, E-mail: rmemon@eng.utah.edu

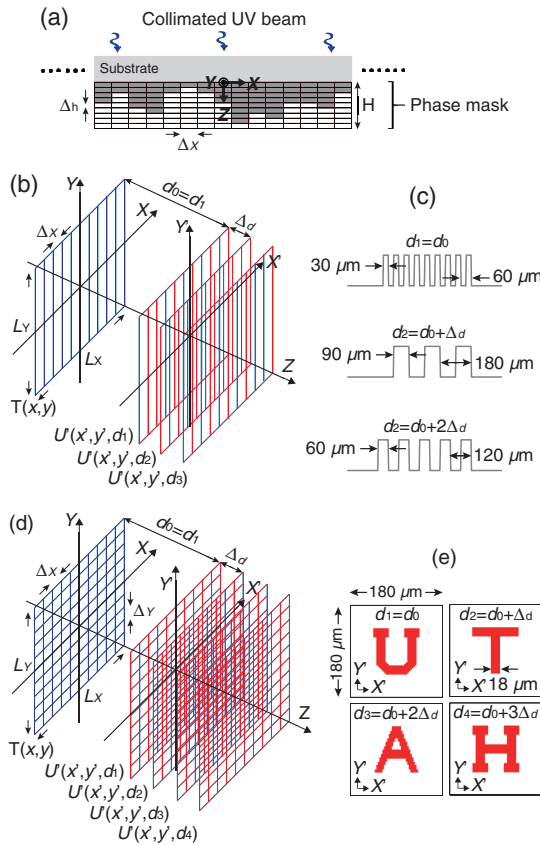


Fig. 1 (a) Schematic of the cross-sectional view of a one-dimensional (1-D) diffractive phase mask. (b) Schematic of microlithography on multiple planes by a 1-D mask, (d) and a two-dimensional (2-D) mask. Intensity distributions U' are generated at distances separated by Δd . (c) Target exposure images at three planes: nine lines at $z = d_1 = d_0 = 80$ mm with 30- μm linewidth and 60 μm spacing; three lines at $z = d_1 = d_0 + \Delta d = 81$ mm with 90 μm linewidth and 180 μm spacing; five lines at $z = d_1 = d_0 + 2\Delta d = 82$ mm with 60 μm linewidth and 120 μm spacing. (e) Target exposure images with 180 $\mu\text{m} \times 180 \mu\text{m}$ period at four planes: letter “U” at $z = d_1 = d_0 = 5.0$ mm; letter “T” at $z = d_1 = d_0 + \Delta d = 5.3$ mm; letter “A” at $z = d_1 = d_0 + 2\Delta d = 5.6$ mm; letter “H” at $z = d_1 = d_0 + 3\Delta d = 5.9$ mm. Linewidth is 18 μm .

heights, which are uniformly quantized by a unit height Δh . In its 1-D form [Fig. 1(a)], Δx denotes its uniform pixel size. The diffractive mask was fabricated into a polymer layer using grayscale lithography^{21,22,26,30} on a laser-pattern generator. Since the resolution of this process was limited to 3 μm , we constrained all our mask designs to pixels of size 3 μm or larger. The maximum thickness of the polymer layer H (and hence, of each pixel in the array) was chosen so as to achieve the maximum phase shift of 2π . For a polymer refractive index of 1.76 and illumination wavelength of 325 nm, this corresponded to 430 nm.

Two mask designs in 1-D [Figs. 1(b) and 1(c)] and 2D [Figs. 1(d) and 1(e)] were optimized. The light intensity patterns at multiple planes (or in 3-D volume) $U'(x', y', d)$ can be derived based on the transmission function of the mask $T(x, y)$, which describes phase modulation. In the 1-D case, the desired patterns are three groups of periodic lines. Linewidths of 30, 90, 60 μm and spacings of 60, 180, and 120 μm are designated at $z = d_1 = d_0 = 80$ mm, $z = d_2 = d_0 + \Delta d = 81$ mm and $z = d_2 = d_0 + 2\Delta d = 82$ mm, respectively [see Fig. 1(c)]. The mask is $L_x = 3$ mm

long (1000 pixels). Each pixel is quantized into 32 levels such that $\Delta h = 13.9$ nm. The 2-D target patterns are “U,” “T,” “A,” and “H” letters separated by a gap of $\Delta d = 0.3$ mm with an initial distance of $d_0 = 5$ mm [see Fig. 1(e)]. 18- μm wide lines are used to draw the patterns. Since they are periodic, each unit cell has dimension of $L_x \times L_y = 180 \mu\text{m} \times 180 \mu\text{m}$ (60 \times 60 pixels). The 2-D phase mask has square pixel with $\Delta x = \Delta y = 3 \mu\text{m}$ and unit height of $\Delta h = 6.8$ nm (64 levels). Ridges in Fig. 1(c) and red parts in Fig. 1(e) stand for places to be exposed in positive-tone photoresist. Note that XY and $X'Y'$ coordinates are employed in the mask space and the image space, respectively.

3 Exposure Results

In Fig. 2, the 1-D diffractive phase mask was designed to project three groups of lines of varying widths and spacings onto three planes positioned at $z = 80, 81,$ and 82 mm, respectively. The target images are summarized in Fig. 1(c). Since these patterns have no variations in the Y direction, they could be exposed onto a plane tilted at 45 deg, instead of three exposures at three planes. In this way, it is also possible to record all the intensity patterns along the Z direction. The optimized phase mask topography is plotted in Fig. 2(b). Figure 2(c) shows an optical micrograph of the fabricated mask along with an atomic-force micrograph of the region delimited by the black rectangle. The multiple height levels and the discrete pixels are clearly visible. The simulated light intensity in the $X'Z$ plane from $z = 78.5$ to $z = 83.5$ mm is shown in Fig. 2(d). At the design planes corresponding to $z = 80, 81,$ and 82 mm, the patterns corresponding to 9 lines (period = 60 μm), 3 lines (period = 180 μm), and 5 lines (period = 120 μm), respectively, are clearly visible. The optical efficiency, η in one plane, is defined as the ratio of the energy within the desired pattern to the total energy incident on the mask. The calculated optical efficiencies are denoted in the figure. The samples for lithography were silicon wafers coated with a 1.3- μm -thick photoresist (Shipley 1813) and mounted on a holder that was placed at 45 deg to the optical axis. The illumination power density at the mask plane was 0.635 mW/cm^2 and the exposure time was 90 s. The sample was developed in 352 developer for 60 s. Optical micrographs of the patterns corresponding to the regions close to the planes at $z = 80, 81,$ and 82 mm [rectangular blocks of yellow-broken lines in Fig. 2(d)] are shown in Figs. 1(e)–1(g), respectively. Excellent agreement with the simulation results is seen. The linewidths at three z positions (80, 81, and 82 mm) are 34, 100, and 65 μm , respectively, which indicate the deviation of +4, +10, and +5 μm . These errors, together with the undesired exposures outside the designated line regions, are partially ascribed to overexposure. The simulated light intensity at three positions is plotted as blue lines beside the micrographs in Figs. 2(e)–2(g). By applying a proper threshold, it is possible to achieve clean lines with accurate widths and suppressed noises (black lines). Subsequently, numerical analysis will show how fabrication errors affect the exposure results. Additionally, a simulated 3 μm line [Fig. 2(h) representing the green box in Fig. 2(d)] was measured roughly 5 μm wide by exposure [Fig. 2(i) representing the green box in Fig. 2(e)].

In the next experiment, another mask was designed to project four letters “U,” “T,” “A,” and “H” onto $X'Y'$ planes

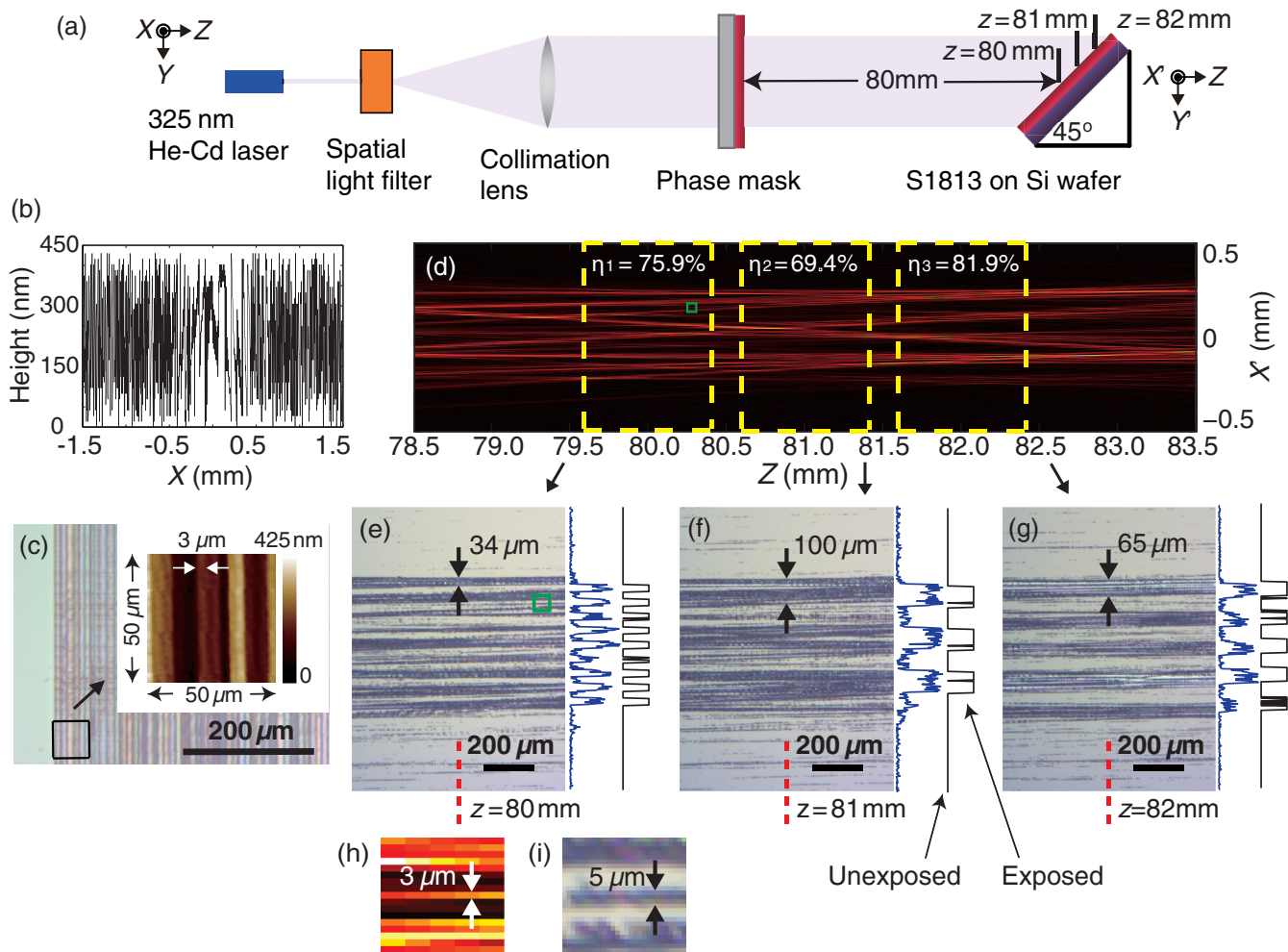


Fig. 2 Lithography on a 45-deg tilted surface. (a) Schematic of the exposure setup. (b) Height profile of the optimized 1-D phase mask. (c) Optical microscope image of one edge of the fabricated phase mask (inset: AFM measurement of a $50\ \mu\text{m} \times 50\ \mu\text{m}$ region, and $\Delta x = 3\text{-}\mu\text{m}$ pixel size is labeled). (d) Simulated intensity distribution in the $X'Z$ plane, where Z is the direction of light propagation. Optical efficiencies at three planes are given. (e)–(g) Optical micrographs of the exposed and developed results at three regions enclosed by yellow blocks in (d). Measured linewidths at (e) $z = 80$, (f) $z = 81$ and (g) $z = 82$ mm are 34 , 100 , and $65\ \mu\text{m}$, respectively. Blue lines are simulated intensity distributions at three planes and black lines represent the estimated exposure outcomes by applying a proper threshold to the simulated patterns. (h) and (i) Magnified views of small areas delimited by the green boxes in (d) and (e), respectively. The labeled $3\ \mu\text{m}$ line in (h) is experimentally measured $5\ \mu\text{m}$.

corresponding to $z = 5$, 5.3 , 5.6 , and 5.9 mm, respectively, as illustrated in Fig. 3(a). Figure 3(b) gives the topography of the designed mask. An optical micrograph of the fabricated mask along with an atomic-force micrograph of a small region is shown in Fig. 3(c). The multiple height levels of the square pixels are evident. Simulated light intensity distributions in the $X'Y'$ planes at the four planes are plotted in Figs. 3(d)–3(g). The corresponding optical efficiencies are also denoted in the figures. The measured optical intensity at the mask plane was $0.734\ \text{mW}/\text{cm}^2$ and the sample was exposed for 52 s. Optical micrographs of the corresponding exposed and developed patterns are shown in Figs. 3(h)–3(k). The experimental results agree very well with the simulation predictions. 21, 20, and $19\ \mu\text{m}$ widths are obtained for the 18 μm lines by measurements. Arrays of the patterned letters are given by microscope images in Figs. 3(l)–3(o). The noise present in the exposure results

in Figs. 3(d)–3(g) are likely due to both overexposure and mask fabrication errors. Figures 3(p) and 3(q) show the exposure patterns predicted by implementing high (critical exposure) and low (overexposure) thresholds to the simulated light intensity distributions in Figs. 3(d)–3(g). Compared to Fig. 3(p), Fig. 3(q) clearly includes more noise and approaches the experimental results in Figs. 3(h)–3(k) with better accuracy.

In a third experiment, the sample substrate was placed orthogonal to the diffractive mask as illustrated in Fig. 4(a). For simplicity, the same phase mask as in Fig. 3 was used. The simulated light intensity distribution in the $X'Z$ plane is shown in Fig. 4(c) and the optical micrograph of the exposed and developed pattern is shown in Figs. 4(d) and 4(e). The pattern corresponds to the lower part of the four characters, i.e., the fat line at the bottom of “U” ($z = 5$ mm), the center line of “T” ($z = 5.3$ mm), the legs at

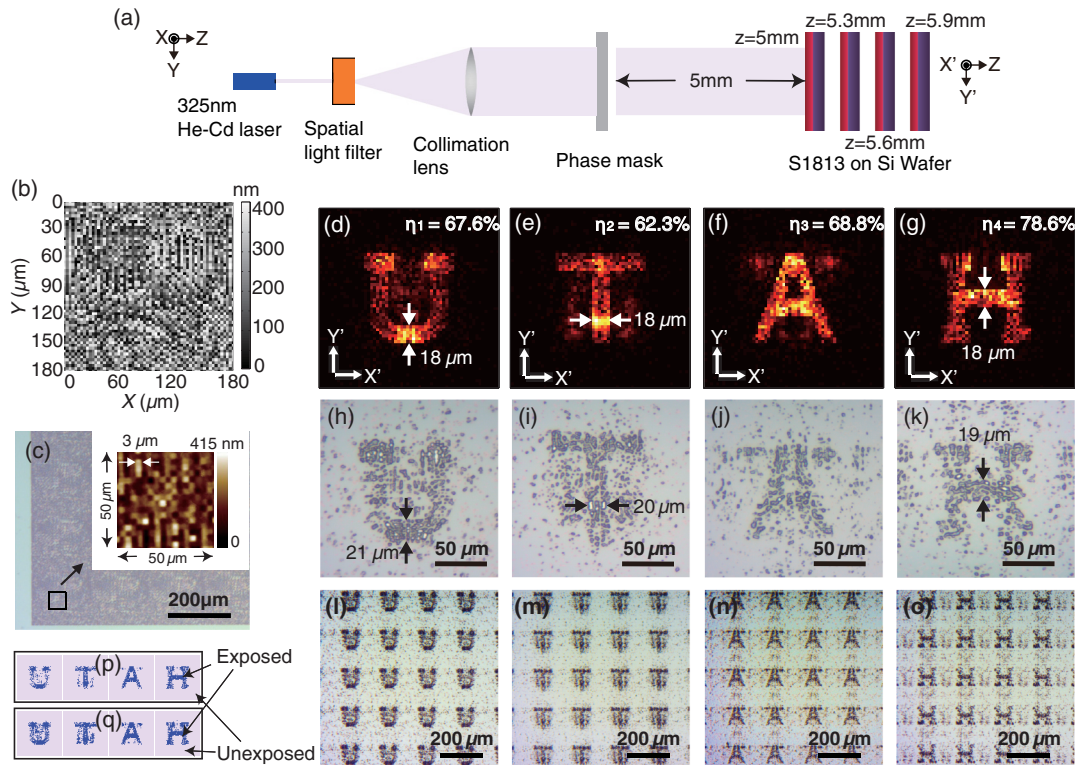


Fig. 3 Lithography on multiple planes parallel to the mask. (a) Schematic of the exposure setup. (b) Height profile of the optimized 2-D phase mask. (c) Optical microscope image of one corner of the fabricated periodic phase mask (inset: AFM measurement of a $50\ \mu\text{m} \times 50\ \mu\text{m}$ region, and $3\text{-}\mu\text{m}$ pixel size is labeled). (d)–(g) Simulated intensity distributions of one period on the $X'Y'$ plane. Optical efficiencies are given. (h)–(k) Optical micrographs of the exposed and developed results of one period. Designed $18\ \mu\text{m}$ lines have measured linewidths of 21 , 20 , and $19\ \mu\text{m}$, respectively. (l)–(o) Optical micrographs of the exposed and developed results of the periodic arrays. (d), (h) and (l) are letter “U” at $z = 5.0\ \text{mm}$. (e), (i) and (m) are letter “T” at $z = 5.3\ \text{mm}$. (f), (j) and (n) are letter “A” at $z = 5.6\ \text{mm}$. (g), (k) and (o) are letter “H” at $z = 5.9\ \text{mm}$. Estimated exposure results by applying high (p) and low (q) thresholds.

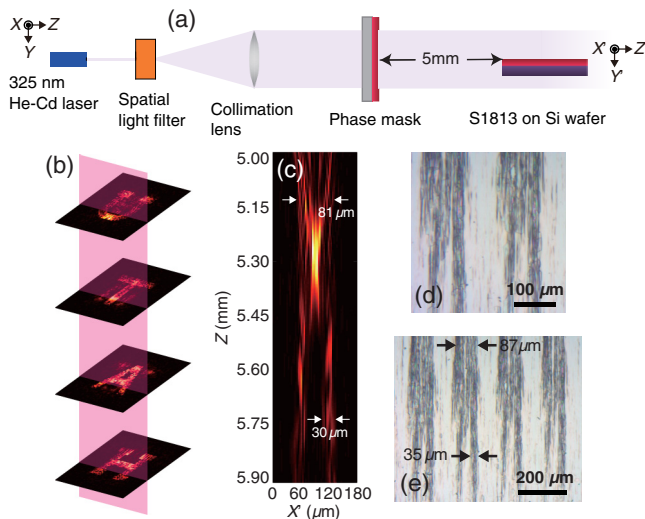


Fig. 4 Lithography on a surface orthogonal to the mask. (a) Schematic of the exposure setup. (b) Schematic illustrating that the exposure plane (pink) is the $X'Z$ cross section of the intensity pattern of the phase mask that generates “U” “T” “A” “H” letters. (c) Simulated intensity distribution on the $X'Z$ plane [pink surface in (b)]. Optical micrographs of the exposed and developed results of two (d) and four (e) periods. Simulated 81 and $30\ \mu\text{m}$ lines in (c) have measured linewidths of 87 and $35\ \mu\text{m}$ in (e), respectively.

the bottoms of “A” and “H” ($z = 5.6\ \text{mm}$ and $z = 5.9\ \text{mm}$). A cross-sectional schematic is depicted in Fig. 4(b). Note that several periods (spacing of $180\ \mu\text{m}$) of the design in Fig. 4(b) were fabricated on the mask. This resulted in repeated patterns as indicated in Figs. 4(d) and 4(e). The agreement between the two patterns indicates that the diffractive mask is capable of patterning onto surfaces of extreme obliqueness. In this case, the surface is perpendicular to the diffractive mask. The measured laser intensity at the diffractive mask was $0.748\ \text{mW}/\text{cm}^2$ and the exposure time was $30\ \text{min}$. The exposure time is significantly increased compared to Fig. 3 due to the large angle between the light propagation direction and the surface of the photoresist. Nevertheless, patterns with micron-scale fidelity can be achieved. Simulated features of 81 and $30\ \mu\text{m}$ [Fig. 4(c)] are 87 and $35\ \mu\text{m}$ wide [Fig. 4(e)] because of overexposure and mask fabrication error.

Additionally, it is instructive to design a phase mask for exposure on a highly oblique surface. Figure 5 summarizes the numerical results of an optimized 1-D phase mask that is designed to expose three narrow regions ($\sim 6\ \mu\text{m}$ width) spaced by 0.3 and $0.9\ \text{mm}$ in X' and Z directions, respectively. It contains 1000 pixels of $3\ \mu\text{m}$ width; the mask is $3\ \text{mm}$ long. It has a maximum height of $600\ \text{nm}$ and unit height of $10\ \text{nm}$ (61 levels). The first exposure plane is $30\ \text{mm}$ away from the mask [Fig. 5(a)]. The simulated

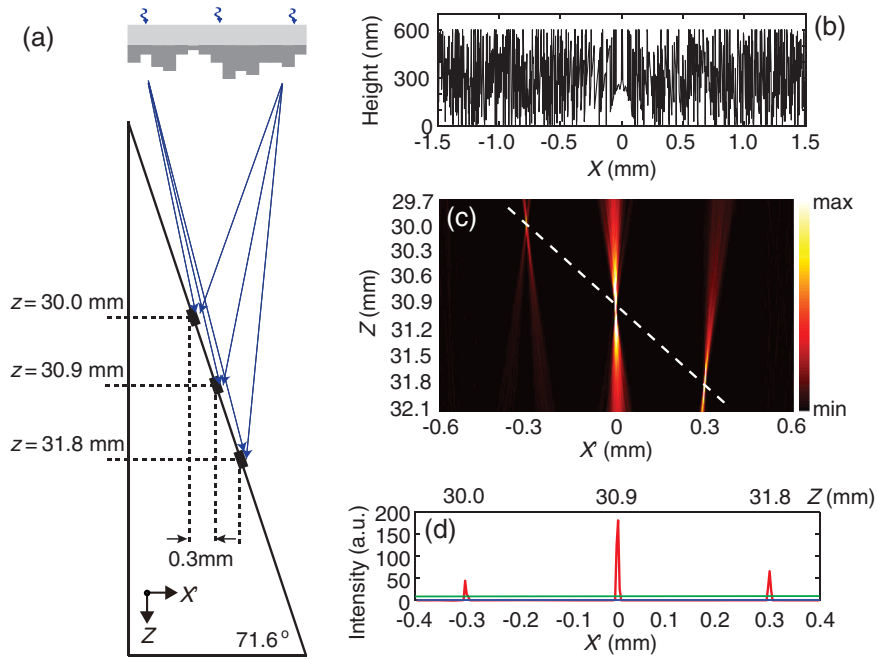


Fig. 5 Design of a 1-D phase mask for exposure on highly oblique surface. (a) Schematic of exposure on a surface of 71.6 deg angle. Three exposed regions, represented by small black blocks, are separated by 0.9 mm axially and 0.3 mm laterally. (b) Height profile of the optimized 1-D phase mask. (c) Simulated light intensity distribution along X' direction and the direction of propagation (Z). White dashed line represents the 71.6 deg tilted surface. (d) Intensity distribution on the 71.6 deg tilted surface [along white dashed line in (c)]. Green line represents exposure threshold.

light intensity distribution shows highly efficient focus spots at the three designated positions in the X'/Z plane [Fig. 5(c)]. By following the white dashed line in Fig. 5(c), light intensity received by the 71.6 deg tilted surface is plotted in Fig. 5(d). After applying a proper threshold (green line), the desired exposure pattern can be produced with excellent accuracy.

4 Discussion

4.1 Fabrication Error

Since the designed mask generates 3-D light field by introducing spatial phase modulation, it is necessary to pattern microstructures as close to the optimized height distribution

as possible. Therefore, it is important to understand how fabrication errors of the diffractive phase mask affects its performance. Figure 6 plots the calculated optical efficiencies where Gaussian noise with zero mean (μ) and various standard deviations (δ) are added to the original design. The efficiencies are reduced with increased standard deviations. Both Figs. 6(a) and 6(b) indicate that errors with standard deviation greater than 100 nm ($\sim 23\%$ of the maximum height 430 nm) lead to meaningless results where noise overwhelms the signal. With $\delta = 40$ nm ($\sim 9\%$ of 430 nm), the 1-D and the 2-D masks have average optical efficiencies decreased from 70% and 60% to 54% and 45%. Insets of Fig. 6(b) include the intensity distribution simulations of the 2-D phase mask with applied errors ($\delta = 5, 40,$ and

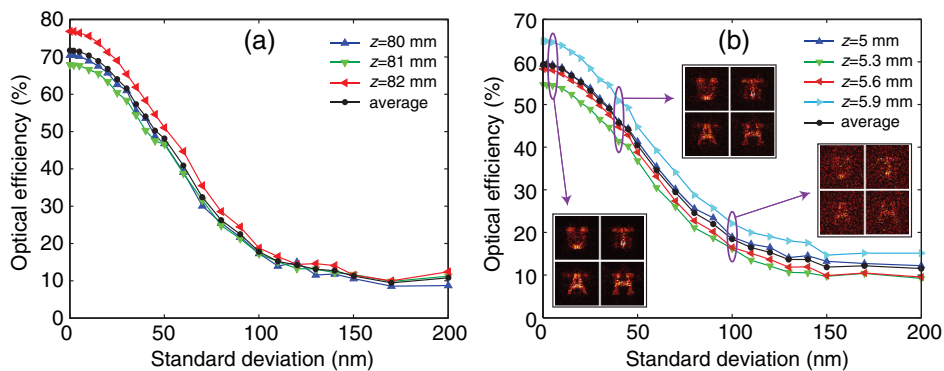


Fig. 6 Optical efficiencies after adding Gaussian noises with zero mean and standard deviations from 0 to 200 nm to the height distributions of the (a) 1-D and (b) 2-D phase masks. They are calculated at the designated exposure planes and take the average (black lines). Insets of (b): simulated light intensity distributions at four planes separated by 0.3 mm with low noise of $\delta = 5$ nm (left), medium noise of $\delta = 40$ nm (middle), and high noise of $\delta = 100$ nm (right).

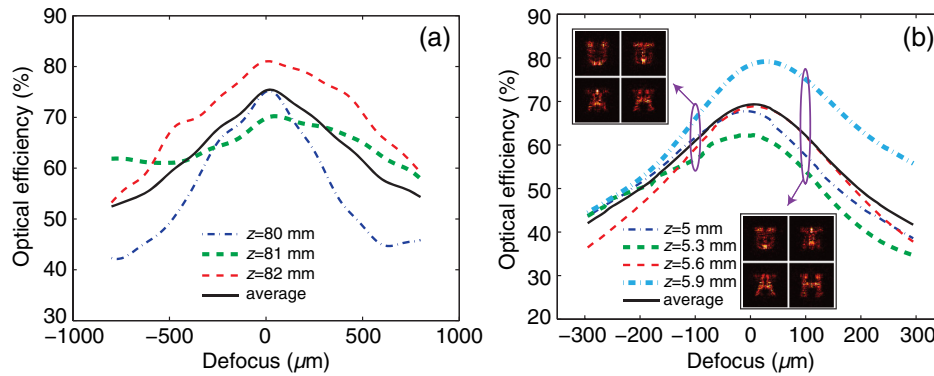


Fig. 7 Optical efficiencies at various defocus locations of the (a) 1-D and (b) 2-D phase masks. They are calculated at different exposure planes and take the average (black lines). Insets of (b): simulated light intensity distributions at four planes separated by 0.3 mm at $-100 \mu\text{m}$ defocus (left) and $+100 \mu\text{m}$ defocus (right).

100 nm). 5-nm error has trivial effect on the signal-to-noise ratio. However, with 40-nm error the patterns start to lose their accuracy. This also explains the undesired exposures observed in Figs. 2(e)–2(g) and Figs. 3(h)–3(k), which occurred outside the designated regions [defined in Figs. 1(c) and 1(e)]. Based upon measurements, the height error in our grayscale lithography is about 30 nm. Hence, it is critical to suppress fabrication errors, especially $\delta < 40$ nm, by accurate calibration, process parameter optimization, and better condition control.

4.2 Resolution

The spatial resolution by the proposed lithography technique is primarily defined by the fabrication resolution of the phase mask. In this paper, we exploited the Heidelberg microPG101 machine with 3- μm mode write-head for grayscale patterning ($\Delta x = \Delta y = 3 \mu\text{m}$). Theoretically, the attainable resolution by OPL is defined by $C.D. = k_1 \lambda / \text{NA}$, in which λ is the illumination wavelength, NA is the numerical aperture of the projection lens, and k_1 is a system-related scale coefficient.^{31–33} For a pixelated phase mask $\text{NA} \approx \lambda / 2\Delta x$. Usually, k_1 takes a value of 0.5, which results in a resolution $C.D. \approx \Delta x$. In Figs. 2(h) and 2(i), a simulated 3 μm line was measured 5 μm wide due to overexposure and the limited resolution of the optical microscope. Similarly, the other measured line-widths are within +15% of the nominal values. Therefore, by optimizing exposure condition and minimizing mask fabrication error, it is possible to approach the predicted resolution. Additionally, smaller features can be achieved once an advanced mask generation tool is utilized (down to $< 1 \mu\text{m}$ resolution).

4.3 Defocus

Depth-of-focus (DOF) is another issue considered in OPL systems. Generally, a projection lens has a DOF determined by $\text{DOF} = k_2 \lambda / \text{NA}^2 = 4k_2 \Delta x^2 / \lambda$, in which k_2 is another system-related factor.^{32–34} Assuming $k_2 = 0.5$, $\text{DOF} = 55 \mu\text{m}$ for a $\lambda = 325$ nm laser with $\Delta x = 3 \mu\text{m}$. Contrary to conventional 2-D lithography, a shorter DOF is desired in micropatterning on oblique and multiplane surfaces, since more pattern changes are expected within a certain distance. This can be realized by reducing the pixel size of the phase mask and using a long-wavelength

light source. The optical efficiencies at various defocus planes are plotted in Fig. 7. The efficiencies drop to 60% at ± 500 and $\pm 100 \mu\text{m}$ defocus for both 1-D [Fig. 7(a)] and 2-D [Fig. 7(b)] masks. At the $-100 \mu\text{m}$ plane [top inset of Fig. 7(a)], the letters “U” and “T” have well-preserved patterns, while the other two exhibit obvious distortions. On the other hand, “A” and “H” look good, while the first two have worsened shapes at the $+100 \mu\text{m}$ plane [bottom inset of Fig. 7(b)]. Thus, in exposure experiments, it is crucial to control the gap between the mask and the sample as close to the designed value as possible.

5 Conclusions

Managing light intensities in 3-D space using broadband diffractive optics allows for a new and efficient technique to pattern microstructures on oblique and multiplane surfaces. Clearly, this technique can be extended to conventional 3-D lithography. Compared to scanning two-photon lithographic techniques, the reported method is based on a single optical exposure and effectively avoids high-power pulsed lasers and slow scanning schemes.^{34,35} Our technique can be readily adapted for high-throughput manufacturing. The diffractive phase mask allows for a large number of degrees-of-freedom, which permits generation of complex geometries in 3-D space. The technique currently suffers from crosstalk between the patterns as is evident in Figs. 3(d)–3(g). This effect can be reduced by the use of smaller fabrication pixels, which will provide many more pixels, and hence more degrees-of-freedom for the optimization algorithm. Shrinking pixel size also helps in improving patterning resolution. Furthermore, our previous work in broadband diffractive optics²⁰ indicates that with a larger number of pixels, the sensitivity of the projected pattern to pixel errors is also minimized. One challenge in the reported method is that the resolution in the Z-axis is limited by the DOF of the diffractive-optical mask. Distances between the exposure planes that are several multiples of this DOF are necessary to effectively separate different patterns. The DOF can be decreased by using smaller pixels and longer wavelengths. In addition, the computer-generated micro-optic device can be faithfully replicated, and thus mass-produced via roll-to-roll nanoimprint.¹⁸ The next step is to explore its vast capabilities in 3-D micropatterning.

Acknowledgments

The authors would like to thank Brian Baker at the Utah Nanofabrication Facility for assistance with grayscale lithography process, and Brian van Devenner for help with atomic force microscopy (AFM) imaging. We also thank Apratim Majumder for assistance with the exposure setup. Jose Dominguez-Caballero and Ganghun Kim are also acknowledged for their earlier work on the optimization algorithm.

References

1. J. D. Joannopoulos, P. R. Villeneuve, and S. H. Fan, "Photonic crystals: putting a new twist on light," *Nature* **386**, 143–149 (1997).
2. M. Campbell et al., "Fabrication of photonic crystals for the visible spectrum by holographic lithography," *Nature* **404**, 53–56 (2000).
3. R. S. Patti, "Three-dimensional integrated circuits and the future of system-on-chip design," *Proc. IEEE* **94**, 1214–1224 (2006).
4. N. Miki et al., "Multi-stack silicon-direct wafer bonding for 3-D MEMS manufacturing," *Sens. Actuators A* **103**, 194–201 (2003).
5. E. Verpoorte and N. F. De Rooij, "Microfluidics meets MEMS," *Proc. IEEE* **91**, 930–953 (2003).
6. S. Egashira and E. Nishiyama, "Stacked microstrip antenna with wide bandwidth and high gain," *IEEE Trans. Antennas Propag.* **44**, 1533–1534 (1996).
7. R. Want, "An introduction to RFID technology," *IEEE Pervasive Comput.* **5**, 25–33 (2006).
8. D. Schurig et al., "Metamaterial electromagnetic cloak at microwave frequencies," *Science* **314**, 977–980 (2006).
9. H. Chen, C. Chan, and P. Sheng, "Transformation optics and metamaterials," *Nat. Mater.* **9**, 387–396 (2010).
10. M. J. Booth et al., "Adaptive aberration correction in a confocal microscope," *Proc. Natl. Acad. Sci. U. S. A.* **99**, 5788–5792 (2002).
11. C. Kim et al., "Integrated wireless interface based on the Utah electrode array," *Biomed. Microdevices* **11**, 453–466 (2009).
12. J. John et al., "Microfabrication of 3-D neural probes with combined electrical and chemical interfaces," *J. Micromech. Microeng.* **21**, 105011 (2011).
13. A. W. Martinez, S. T. Phillips, and G. M. Whitesides, "Three-dimensional microfluidic devices fabricated in layered paper and tape," *Proc. Natl. Acad. Sci. U. S. A.* **105**, 19606–19611 (2008).
14. T. Ito and S. Okazaki, "Pushing the limits of lithography," *Nature* **406**, 1027–1031 (2000).
15. J. A. Dominguez-Caballero, S. Takahashi, and G. Barbastathis, "Design and sensitivity analysis of Fresnel domain computer generated holograms," *Int. J. Nanomanuf.* **6**, 207 (2010).
16. M. Galus et al., "Replication of diffractive-optical arrays via photocurable nanoimprint lithography," *J. Vac. Sci. Technol. B* **24**, 2960–2963 (2006).
17. K. S. Chen, I. K. Lin, and F. H. Ko, "Fabrication of 3-D polymer microstructures using electron beam lithography and nanoimprinting technologies," *J. Micromech. Microeng.* **15**, 1894–1903 (2005).
18. L. J. Guo, "Nanoimprint lithography: methods and material requirements," *Adv. Mater.* **19**, 495–513 (2007).
19. J. G. Goodberlet and B. L. Dunn, "Deep-ultraviolet contact photolithography," *Microelectron. Eng.* **53**, 95–99 (2000).
20. G. Kim, J. A. Dominguez-Caballero, and R. Menon, "Design and analysis of multi-wavelength diffractive optics," *Opt. Express* **20**, 2814–2823 (2012).
21. P. Wang et al., "A new class of multi-bandgap high efficiency photovoltaics enabled by broadband diffractive optics," *Prog. Photovoltaic: Res. Appl.* (2014).
22. P. Wang et al., "Hyper-spectral imaging in scanning-confocal-fluorescence microscopy using a novel broadband diffractive optic," *Opt. Commun.* **324**, 73–80 (2014).
23. G. Kim and R. Menon, "An ultra-small 3-D computational microscope," *Appl. Phys. Lett.* **105**, 061114 (2014).
24. P. Wang and R. Menon, "Optimization of periodic nanostructures for enhanced light-trapping in ultra-thin photovoltaics," *Opt. Express* **21**, 6274–6285 (2013).
25. P. Wang and R. Menon, "Optimization of generalized dielectric nanostructures for enhanced light trapping in thin-film photovoltaics via boosting the local density of optical states," *Opt. Express* **22**, A99–A110 (2014).
26. P. Wang and R. Menon, "Computational spectroscopy based on a broadband diffractive optic," *Opt. Express* **22**, 14575–14587 (2014).
27. M. A. Seldowitz, J. P. Allebach, and D. W. Sweeney, "Synthesis of digital holograms by direct binary search," *Appl. Opt.* **26**(14), 2788–2798 (1987).
28. T. R. M. Sales and D. H. Raguin, "Multiwavelength operation with thin diffractive elements," *Appl. Opt.* **38**(14), 3012–3018 (1999).
29. B. Kress and P. Meyrueis, *Digital Diffractive Optics: An Introduction to Planar Diffractive Optics and Related Technology*, John Wiley, New York (2000).
30. K. Totsu et al., "Fabrication of three-dimensional microstructure using maskless gray-scale lithography," *Sens. Actuators A* **130**, 387–392 (2006).
31. S. Okazaki, "Resolution limits of optical lithography," *J. Vac. Sci. Technol. B* **9**, 2829–2833 (1991).
32. H. Wang et al., "Spot size and depth of focus in optical data storage system," *Opt. Eng.* **46**(6), 065201 (2007).
33. B. J. Lin, "The k_3 coefficient in nonparaxial λ/NA scaling equations for resolution, depth of focus, and immersion lithography," *J. Micro/Nanolith. MEMS MOEMS* **1**(1), 7–12 (2002).
34. S. Maruo, O. Nakamura, and S. Kawata, "Three-dimensional microfabrication with two-photon-absorbed photopolymerization," *Opt. Lett.* **22**, 132–134 (1997).
35. W. Zhou et al., "An efficient two-photon-generated photoacid applied to positive-tone 3-D microfabrication," *Science* **296**, 1106–1109 (2002).

Peng Wang is currently a PhD candidate in the Electrical and Computer Engineering Department at the University of Utah. He received his bachelor's degree in optical engineering from Zhejiang University, China, in 2011. His research is focused on modeling, fabrication, and characterization of diffractive micro-optics and its applications in photovoltaics, spectroscopy, imaging, and lithography. He is also interested in nanophotonics and computational optics.

Rajesh Menon received his SM and PhD degrees from MIT. His research is focused on nanofabrication, computation, and photonics to innovate in super-resolution lithography, metamaterials, diffractive optics, integrated photonics, photovoltaics, and computational optics. His research has yielded over 70 publications, 30 patents, and 2 companies. Among his honors are the NASA Early Stage-Innovations Award, the NSF CAREER Award, and the International Commission for Optics Prize. Currently, he is the director of the Laboratory for Optical Nanotechnologies at the University of Utah.